

# Magnetic field induced reentrant multipolar ordering in the distorted kagome-lattice antiferromagnet $\text{Dy}_3\text{Ru}_4\text{Al}_{12}$

Isao Ishii\* and Takashi Suzuki†

*Department of Quantum Matter, AdSE, Hiroshima University, Higashi-Hiroshima 739-8530, Japan*Alexander V. Andreev *FZU Institute of Physics, Czech Academy of Sciences, Na Slovance 2, 182 21 Prague, Czech Republic*

Keisuke Mitsumoto

*Liberal Arts and Sciences, Faculty of Engineering, Toyama Prefectural University, Imizu, Toyama 939-0398, Japan*

Koji Araki

*Department of Applied Physics, National Defense Academy, Yokosuka, Kanagawa 239-8686, Japan*

Atsuhiko Miyata, Denis I. Gorbunov, Sergei Zherlitsyn, and J. Wosnitza

*Hochfeld-Magnetlabor Dresden (HLD-EMFL) and Würzburg-Dresden Cluster of Excellence ct.qmat, Helmholtz-Zentrum Dresden-Rossendorf, 01328 Dresden, Germany*

(Received 2 April 2023; accepted 9 May 2023; published 18 May 2023)

We report on ultrasonic and magnetocaloric-effect measurements of the hexagonal antiferromagnet  $\text{Dy}_3\text{Ru}_4\text{Al}_{12}$  having a distorted kagome lattice. We observed a pronounced softening of the transverse modulus,  $C_{44}$ , above 30 T applied along [100], indicating an as-yet-unidentified magnetic field induced phase transition. We determined the field-temperature phase diagrams using pulsed magnetic fields up to 55.2 T, applied along [100] and [001]. Optimizing crystal-electric-field parameters within the mean-field approximation, we conclude that the enhancement of the field induced phase-transition temperature is due to electric quadrupolar and magnetic octupolar mediated interactions. We propose that the order parameter of the magnetic field induced phase transitions is the electric quadrupole  $O_{2x}$ , facilitated by octupole-mediated interactions.

DOI: [10.1103/PhysRevB.107.205136](https://doi.org/10.1103/PhysRevB.107.205136)

## I. INTRODUCTION

Antiferromagnetically interacting spins on a triangular lattice, such as the kagome lattice, have attracted much attention in terms of fascinating magnetic properties due to geometrical frustration [1,2]. Furthermore, rare-earth compounds with localized  $f$  electrons present intriguing physical properties originating from spin and orbital degrees of freedom, such as multipolar ordering [3–5]. The hexagonal compounds  $R_3\text{Ru}_4\text{Al}_{12}$  ( $R$  = rare earth) have the  $\text{Gd}_3\text{Ru}_4\text{Al}_{12}$ -type structure (space group  $P6_3/mmc$ ), and the  $R$  ions form a distorted kagome lattice in the (001) planes [6,7]. For instance, the Gd-based compound  $\text{Gd}_3\text{Ru}_4\text{Al}_{12}$  shows a complex magnetically ordered structure, which was reported to be a sinusoidal-helical ordering [8,9]. We have recently studied the  $R_3\text{Ru}_4\text{Al}_{12}$  series for its magnetism and multipole-mediated interactions, including the effect of geometrical frustration [10–20].

The Dy-based metallic compound  $\text{Dy}_3\text{Ru}_4\text{Al}_{12}$  undergoes antiferromagnetic (AFM) ordering at  $T_N = 7$  K. The transition is first-order evidenced by the specific heat and thermal expansion

measurements [16,17]. Neutron-diffraction experiments reveal a noncollinear ordered structure with a propagation vector  $(1/2\ 0\ 1/2)$  below  $T_N$  [16]. Gao *et al.* reported further noncoplanar spin trimers with local spin chirality [21].

The  $4f$  electrons in  $\text{Dy}_3\text{Ru}_4\text{Al}_{12}$  possess a localized character. The magnetic anisotropy in this compound is caused by the crystal electric field (CEF) [16,18]. The  $\text{Dy}^{3+}$  16-fold multiplet (total angular momentum  $J = 15/2$ ) splits into eight Kramers doublets in the hexagonal CEF. We previously performed a CEF analysis for reproducing the transverse elastic modulus,  $C_{44}$ , and magnetic susceptibilities. From that, we obtain the ground-state Kramers doublet, the first excited doublet at 8 K, the second excited doublet at 16 K, and the third excited doublet at 21 K [18].

We also observed a magnetic field induced phase transition when applying the magnetic field along the [100] and [001] directions by means of ultrasonic measurements [18]. We note that the ultrasonic technique is an effective tool to investigate quadrupole-mediated interactions because a strain induced by ultrasound bilinearly couples to a corresponding quadrupole moment [22–33]. The significant elastic softening of  $C_{44}$  in  $\text{Dy}_3\text{Ru}_4\text{Al}_{12}$  was understood as being due to an interlevel quadrupole-mediated interaction between the ground-state and excited Kramers doublets. Here,  $C_{44}$  is the linear

\*ish@hiroshima-u.ac.jp

†tsuzuki@hiroshima-u.ac.jp

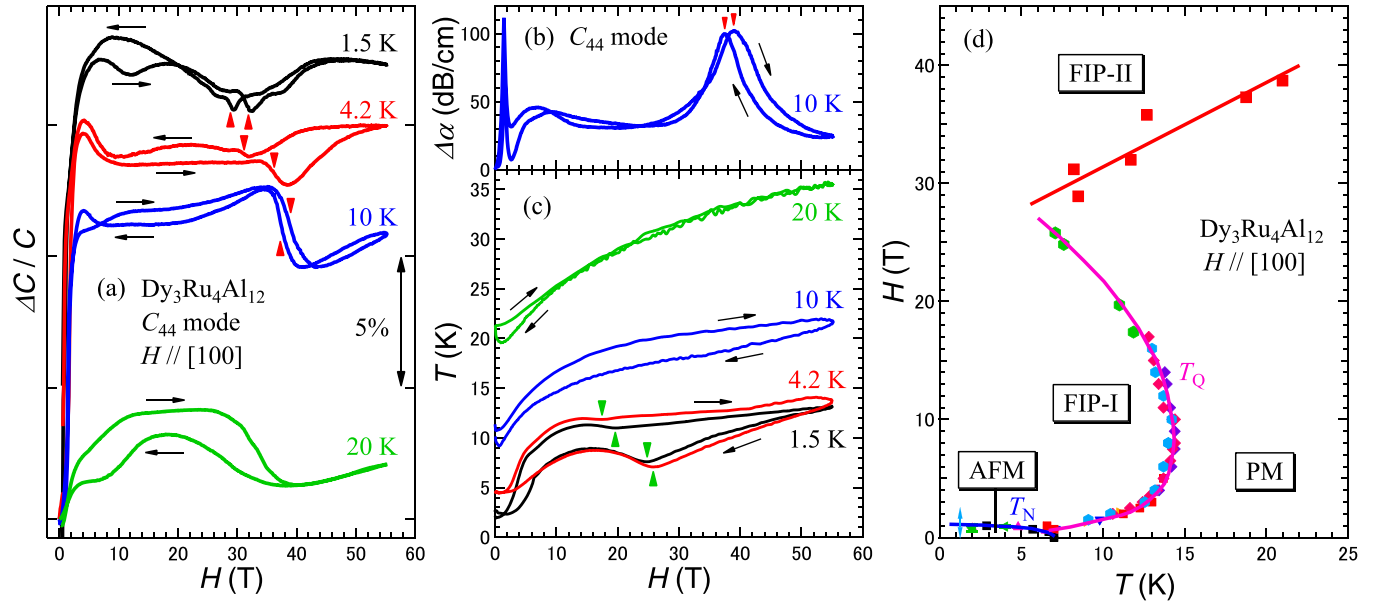


FIG. 1. Magnetic field dependences of (a) the transverse elastic modulus  $C_{44}$ , (b) the ultrasound attenuation for  $C_{44}$  at 10 K, and (c) the magnetocaloric effect for  $\mathbf{H}||[100]$  in  $\text{Dy}_3\text{Ru}_4\text{Al}_{12}$ . The vertical arrowheads indicate a phase transition. The temperatures given in each panel are the starting temperatures of the experiments. (d)  $H$ - $T$  phase diagram for  $\mathbf{H}||[100]$ . The solid curves are guides for the eye. The bidirectional blue arrow indicates a first-order phase transition. PM and FIP represent the paramagnetic state and magnetic field induced phase, respectively.

responses to the  $\varepsilon_{yz}$  and  $\varepsilon_{zx}$  strains which couple to the electric quadrupoles  $O_{yz}$  and  $O_{zx}$ , respectively, in the hexagonal symmetry. The softening of  $C_{44}$  remains even under magnetic fields. It is qualitatively explained by our calculations. We concluded that a plausible origin of the magnetic field induced transition in both field directions is a quadrupolar ordering, with the order parameter being the electric quadrupole  $O_{zx}$  for  $\mathbf{H}||[100]$  and  $O_{yz}$  or  $O_{zx}$  for  $\mathbf{H}||[001]$  [18]. Our CEF analysis manifested an antiferroquadrupolar-type coupling constant between electric quadrupoles on the Dy ions. We also suggested a geometrically frustrated alignment of the electric quadrupoles due to the kagome lattice.

The phase boundaries of the magnetic field induced quadrupolar ordering extend beyond 14 T [18]; however, these are not clarified at further high magnetic fields. In this paper, we investigate the field induced phase boundary and multipole-mediated interactions by means of ultrasonic and magnetocaloric-effect measurements on  $\text{Dy}_3\text{Ru}_4\text{Al}_{12}$  in pulsed magnetic fields applied along [100] and [001]. In consequence, we observe an exceptional magnetic field induced phase transition and discuss its origin by considering multipole-mediated interactions and the effect of geometrical frustration within the CEF approach.

## II. EXPERIMENTAL DETAILS

A single-crystalline  $\text{Dy}_3\text{Ru}_4\text{Al}_{12}$  sample was grown by a modified Czochralski method [16]. We measured the elastic modulus  $C_{44}$ , related to the transverse ultrasound mode with propagation,  $\mathbf{k}||[001]$ , and displacement,  $\mathbf{u}||[100]$ , directions, or vice versa, using an orthogonal phase-detection method [34]. The elastic modulus  $C$  is related to the sound velocity  $v$  by  $C = \rho v^2$ , where  $\rho = 6.427 \text{ g/cm}^3$  is the room-temperature mass density. The ultrasound attenuation was measured

simultaneously. We used  $\text{LiNbO}_3$  transducers with a fundamental resonance frequency of about 30 MHz. Magnetic fields were applied along the [100] and [001] directions up to 17 T by a superconducting magnet and up to 55.2 T by a pulsed magnet at the Dresden High Magnetic Field Laboratory [35]. We also performed magnetocaloric-effect measurements using the same pulsed magnet [36,37]. The resistance of the  $\text{RuO}_2$  thermometer, which was directly put on the sample (thermally contacted), was measured by a standard four-probe method.

## III. RESULTS AND DISCUSSION

### A. Ultrasonic and magnetocaloric-effect measurements

Figure 1(a) shows the magnetic field dependences of the transverse elastic modulus,  $C_{44}$ , in pulsed magnetic fields applied along [100].  $C_{44}$  measured at 1.5 and 4.2 K rapidly increases up to 1.5 T reflecting the phase boundary of  $T_N$ . This hardening is consistent with our previous data obtained in static magnetic fields [18].  $C_{44}$  at 1.5 K hardens up to 10 T and softens gradually above 10 T. With further increasing fields, an obvious softening is detected around 30 T. The characteristic field and magnitude of the softening increase as the starting temperature of the experiment increases up to 10 K. The ultrasound attenuation shows a peak at the field of the largest slope of the softening, i.e., a peak of  $dC/dH$ , such as shown for the data at 10 K [Fig. 1(b)]. We define the field of the largest slope of  $C_{44}$  (the peak of ultrasound attenuation) as the phase-transition field.

Meanwhile,  $C_{44}$  displays large hystereses, suggesting possible temperature changes during the field sweep due to magnetocaloric effects. Therefore we also measured the temperature changes during the pulse using the same pulsed-field magnet. Figure 1(c) shows the magnetic field dependences of

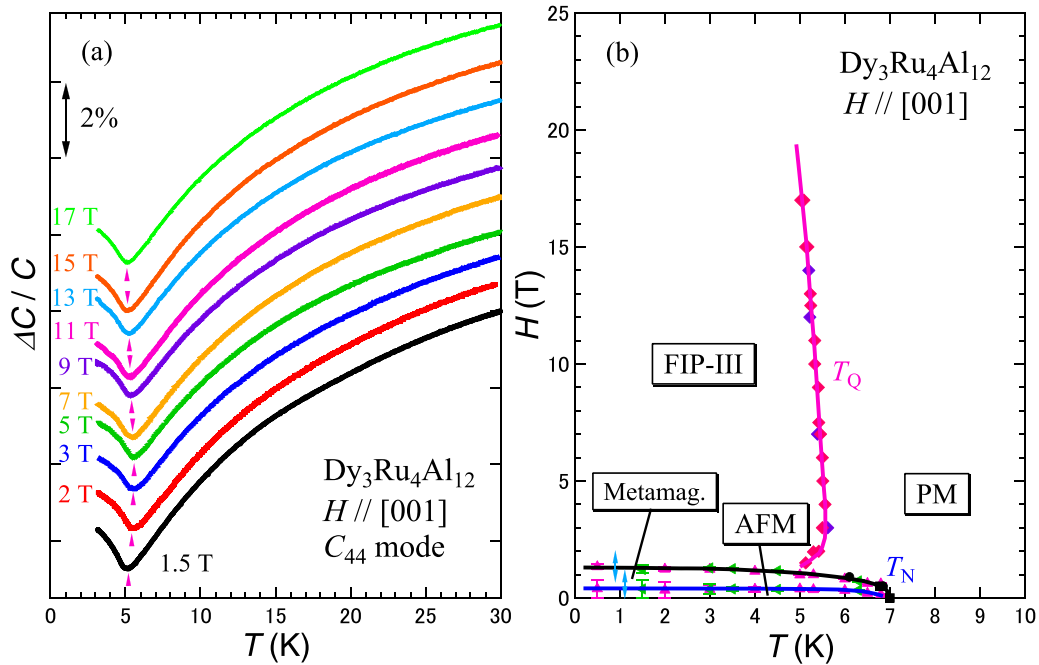


FIG. 2. (a) Temperature dependences of the transverse elastic modulus  $C_{44}$  at elevated magnetic fields in  $\text{Dy}_3\text{Ru}_4\text{Al}_{12}$ . The vertical arrowheads indicate a phase transition. (b)  $H$ - $T$  phase diagram for  $H||[001]$ . The solid curves are guides for the eye. Bidirectional blue arrows indicate first-order phase transitions. Metamag., metamagnetic. (Note that from the careful ultrasonic measurements performed as part of this study, we corrected the phase boundary of FIP-III from the phase diagram previously reported [18].)

the magnetocaloric effect of  $\text{Dy}_3\text{Ru}_4\text{Al}_{12}$  in pulsed magnetic fields applied along [100]. The temperature of the sample increases and decreases in the up and down field sweeps, respectively. In the field sweeps at the starting temperatures of 1.5 and 4.2 K, we observed small dips (green arrowheads), suggesting a phase boundary.

From these results, we map out the  $H$ - $T$  phase diagram for  $H||[100]$  in  $\text{Dy}_3\text{Ru}_4\text{Al}_{12}$  [Fig. 1(d)]. Here, the temperature of the phase-transition field, corresponding to the largest slope of the softening in  $C_{44}$ , was determined using our magnetocaloric-effect measurements. The AFM phase boundary decreases as the field increases and closes around 1 T. We also measured  $C_{44}$  in static fields up to 17 T (not shown) and determined the phase boundary of  $T_Q$  (FIP-I).  $T_Q$  appears around 0.7 T and 7 K, increases up to 10 T (maximum at 14.4 K), decreases above 10 T, and survives up to around 28 T. We previously reported that FIP-I is a quadrupolar ordered phase with order parameter  $O_{zx}$  [18]. It is noteworthy that we discovered an as-yet-unidentified magnetic field induced phase transition to a phase named FIP-II at very high fields applied along [100].

For  $H||[001]$ , we also conducted ultrasonic and magnetocaloric-effect measurements at the starting temperatures 1.5, 4.2, and 13.5 K in pulsed magnetic fields up to 55.2 T.  $C_{44}$  displays large hystereses due to temperature changes. No other phase transition was detected within our experimental conditions (not shown). Because a quadrupolar ordering of  $O_{yz}$  or  $O_{zx}$  was suggested in this field direction [18], we measured  $C_{44}$  at elevated magnetic fields up to 17 T in detail. Figure 2(a) shows the temperature dependences of  $C_{44}$  in static fields applied along [001]. Above 1.5 T,  $C_{44}$  exhibits a large elastic softening when coming from high

temperatures and a sharp minimum around 5 K, reflecting the magnetic field induced phase transition. The temperature of the minimum increases in fields up to 3 T and decreases slightly above 3 T. The minimum is observed even at 17 T with the magnitude of the softening hardly changed. In the static field sweep below 5 K,  $C_{44}$  displays no anomaly up to 17 T, except for the known magnetic phase boundaries at low fields (not shown).

The  $H$ - $T$  phase diagram for  $H||[001]$  in  $\text{Dy}_3\text{Ru}_4\text{Al}_{12}$  is shown in Fig. 2(b). The magnetic phase boundaries close around 0.4 and 1.3 T, respectively.  $T_Q$  appears around 1.5 T and 5 K, increases up to 3 T (maximum at 5.5 K), and decreases above 3 T. The corresponding FIP-III phase extends at least up to 17 T.  $T_Q$  of the phases FIP-I and FIP-III increases at low fields, which can be understood as being due to multipole-mediated interactions. With our measurements, we revealed the  $H$ - $T$  phase diagrams for  $H||[100]$  and  $H||[001]$  up to 55.2 T and discovered an exceptional field induced phase transition for large  $H||[100]$  in  $\text{Dy}_3\text{Ru}_4\text{Al}_{12}$ .

## B. Crystal-electric-field effects

To clarify the origin of the magnetic field induced phase transitions, we first optimized the CEF parameters by analyzing the data of  $C_{44}$ ,  $1/\chi$ , and magnetization  $M$ , starting from CEF data already reported [18]. In the present analysis, we adopted an orthorhombic CEF, because the site symmetry of  $\text{Dy}^{3+}$  is orthorhombic,  $C_{2v}$ , causing magnetic anisotropy in the (001) plane. Also for this symmetry the  $\text{Dy}^{3+}$  16-fold multiplet splits into eight Kramers doublets. We recently pointed out the relevance of a magnetic octupole moment in the kagome-like lattice compounds  $\text{DyNiAl}$  and  $\text{ErNiAl}$ ,

which show a (field induced) quadrupolar ordering in addition to a magnetic ordering at zero magnetic field [38,39]. The magnetic octupoles may facilitate a cross correlation between the ordered spins and quadrupoles in these compounds. We assume that magnetic octupoles also play a role in  $\text{Dy}_3\text{Ru}_4\text{Al}_{12}$ . We consider the following effective Hamiltonian:

$$\begin{aligned}
 H_{\text{eff}} &= H_{\text{CEF}} + H_Q + H_{\text{ex}} + H_{\text{Zeeman}}, \\
 H_{\text{CEF}} &= B_2^0 O_2^0 + B_2^2 O_2^2 + B_4^0 O_4^0 + B_4^2 O_4^2 + B_4^4 O_4^4 \\
 &\quad + B_6^0 O_6^0 + B_6^2 O_6^2 + B_6^4 O_6^4 + B_6^6 O_6^6, \\
 H_Q &= - \sum_i g_i O_i \varepsilon_i - \sum_i g'_i \langle O_i \rangle O_i \quad (i = yz, zx), \\
 H_{\text{ex}} &= - \sum_{j=A,B} \left[ J_{\text{ex}}^{AB} (\langle J_x \rangle^{(j)} J_x + \langle J_y \rangle^{(j)} J_y \right. \\
 &\quad + \langle J_z \rangle^{(j)} J_z) + \sum_i g_{\text{exi}}^{AB} \langle O_i \rangle^{(j)} O_i \\
 &\quad \left. + \sum_k t_{\text{exk}}^{AB} \langle T_z^k \rangle^{(j)} T_z^k \right] \quad (k = \alpha, \beta), \\
 H_{\text{Zeeman}} &= -gJ\mu_B J \cdot H,
 \end{aligned}$$

where  $H_{\text{CEF}}$ ,  $H_Q$ ,  $H_{\text{ex}}$ , and  $H_{\text{Zeeman}}$  are Hamiltonians of the CEF, the quadrupole-mediated interaction, the exchange interaction in the mean-field approximation, and the Zeeman interaction, respectively. Here,  $g_i$  is the strain-quadrupole coupling constant,  $g'_i$  is the quadrupole-quadrupole coupling constant,  $O_i$  is the electric-quadrupole operator,  $T_z^k$  is the magnetic-octupole operator,  $B_m^n$  ( $n = 0, 2, 4, 6$ ;  $m = 2, 4, 6$ ) are the CEF parameters, and  $O_m^n$  are the Stevens equivalent operators [40,41].  $\langle J_x \rangle$ ,  $\langle J_y \rangle$ ,  $\langle J_z \rangle$ ,  $\langle O_i \rangle$ , and  $\langle T_z^k \rangle$  represent thermal averages. The subscripts  $x$ ,  $y$ , and  $z$  of the angular-momentum operator  $J_l$  correspond to [100], [120], and [001], respectively.  $J_{\text{ex}}^{AB}$ ,  $g_{\text{exi}}^{AB}$ , and  $t_{\text{exk}}^{AB}$  are the coupling constants of intersublattice spin, quadrupole, and octupole exchange interactions, respectively, and the symbols  $A$  and  $B$  denote two sublattices [42].

The temperature dependence of  $C_{44}$  in the nonordered state was calculated using the following equation:

$$\begin{aligned}
 C_{44}(T) &= C_0 \left[ \frac{1 - (N_0 g_i^2 / C_0 + g'_i) \chi_s(T)}{1 - g'_i \chi_s(T)} \right], \\
 C_0(T) &= C_{0K} - \frac{s}{\exp(\theta_D/T) - 1}, \quad (1)
 \end{aligned}$$

where  $N_0$  ( $= 9.548 \times 10^{27} \text{ m}^{-3}$ ) is the number of  $\text{Dy}^{3+}$  per unit volume and  $\chi_s$  is the so-called strain susceptibility [43,44]. For the background stiffness,  $C_0(T)$ , we used the Varshni equation, where  $C_{0K}$  is the elastic modulus at 0 K,  $\theta_D$  is the Debye temperature, and  $s$  is a fit parameter [45,46].

TABLE I. CEF parameters of  $\text{Dy}_3\text{Ru}_4\text{Al}_{12}$  in kelvins.

| $B_2^0$ | $B_2^2$               | $B_4^0$               | $B_4^2$                | $B_4^4$               | $B_6^0$                | $B_6^2$                | $B_6^4$                | $B_6^6$               |
|---------|-----------------------|-----------------------|------------------------|-----------------------|------------------------|------------------------|------------------------|-----------------------|
| -0.89   | $8.20 \times 10^{-2}$ | $3.80 \times 10^{-3}$ | $-1.80 \times 10^{-4}$ | $9.00 \times 10^{-4}$ | $-1.60 \times 10^{-5}$ | $-2.60 \times 10^{-5}$ | $-7.70 \times 10^{-6}$ | $2.00 \times 10^{-4}$ |

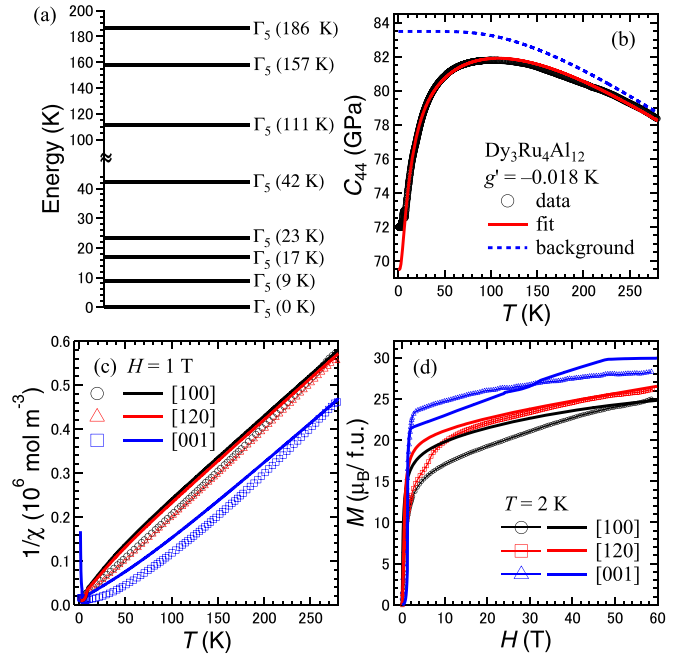


FIG. 3. (a) 4f level scheme for  $\text{Dy}_3\text{Ru}_4\text{Al}_{12}$  obtained from the CEF parameters listed in Table I, where  $\Gamma_5$  denotes the irreducible representation for the point symmetry  $C_{2v}$ . (b) Temperature dependence of the transverse elastic modulus  $C_{44}$ . The red solid and blue dashed curves show the fit result and the background stiffness, respectively. (c) Temperature dependences of the inverse magnetic susceptibility measured at 1 T. (d) Magnetization curves at 2 K. The data are the same as the data previously reported [16]. Solid curves demonstrate the calculated results.

We performed the CEF fits by adding the CEF parameters for orthorhombicity based on the hexagonal CEF reported in Ref. [18]. The energy splitting that we obtained for the CEF-level scheme is almost the same as previously reported, although the CEF parameters for orthorhombicity were added [Fig. 3(a)]. In detail, we obtain the ground-state doublet  $\Gamma_5$ , the first excited doublet  $\Gamma_5$  at 9 K, the second excited doublet  $\Gamma_5$  at 17 K, and many others. The red solid curve in Fig. 3(b) is the best fit of  $C_{44}$  in the nonordered state. The calculated  $C_{44}$  well reproduces the data above  $T_N$  by the fit parameters listed in Tables I and II. As described in our previous paper, the softening of  $C_{44}$  is due to an interlevel quadrupole-mediated interaction between the CEF states, because only the ground-state Kramers doublet generates no elastic softening [18]. The interaction is of antiferroquadrupolar type because of the negative value of  $g'_i$  (Table II).

We calculated  $1/\chi$  and  $M$  including the ordered state by using the CEF model:  $H_{\text{CEF}} + H_{\text{ex}} + H_{\text{Zeeman}}$  [47,48]. For  $H_{\text{ex}}$  the magnetic octupoles,  $T_z^\alpha = (2J_z^3 - J_z J_x^2 - J_x^2 J_z - J_y^2 J_z - J_z J_y^2)/2$  and  $T_z^\beta = \sqrt{15}(J_z J_x^2 + J_x^2 J_z - J_y^2 J_z - J_z J_y^2)/6$  [41],

TABLE II. Fit parameters of  $C_{44}$ :  $|g_i|$  (K),  $g'_i$  (K),  $C_{0K}$  (GPa),  $\theta_D$  (K), and  $s$  (GPa). We used the value of  $\theta_D$  from the specific heat [16].

|          | $ g_i $ | $g'_i$                 | $C_{0K}$ | $\theta_D$ | $s$  |
|----------|---------|------------------------|----------|------------|------|
| $C_{44}$ | 18.0    | $-1.80 \times 10^{-2}$ | 83.5     | 431        | 17.5 |

were adopted for all field directions, because calculations using these two octupoles are consistent with the experimental data within our model. An isotropic  $J_{\text{ex}}^{AB} = -0.24$  K, reflecting the AFM transition, was assumed to simplify the analysis, and we added multipole exchange interactions,  $g_{\text{ex}i}^{AB} = g'_i = -1.80 \times 10^{-2}$  K determined by the fit (Table II) and  $t_{\text{ex}k}^{AB} = -3.00 \times 10^{-4}$  K. These values of  $J_{\text{ex}}^{AB}$  and  $t_{\text{ex}k}^{AB}$  were determined to reproduce  $T_N$  at zero field. Here, the data are better described by negative values of  $g_{\text{ex}i}^{AB}$  and  $t_{\text{ex}k}^{AB}$ . Figures 3(c) and 3(d) show the fit results for  $1/\chi$  in 1 T and  $M$  at 2 K, respectively. The experimental  $1/\chi$  data including magnetic anisotropy are qualitatively reproduced. Below  $T_N$ , the decrease in  $1/\chi$  for  $\mathbf{H}||[100]$  and  $[120]$  and the rapid increase for  $\mathbf{H}||[001]$  in the calculations are consistent with the experimental data [16]. The magnetization data at 2 K including magnetic anisotropy are almost reproduced, except for the phase transition at 7 T for  $\mathbf{H}||[120]$  and around 0.4 T for  $\mathbf{H}||[001]$  [Fig. 3(d)].

### C. Order parameter of magnetic field induced phase transitions

In this section, we discuss the origin of the magnetic field induced phase transitions in both field directions. To

determine the order parameter of the phase transitions, we assessed the phase-transition temperature using the spin, quadrupole, and octupole exchange interactions in the mean-field approximation. The Hamiltonian is the same as that used for calculating  $1/\chi$  and  $M$ . We examined four patterns: the calculated transition temperature employing the magnetic-octupole operator  $T_z^\alpha$ , that employing  $T_z^\beta$ , that employing both  $T_z^k$ , and that employing neither  $T_z^k$ . Here, we also calculated the phase-transition temperature using other magnetic octupoles [41]. Those results are less consistent with the data than the calculations using  $T_z^k$ ; therefore we employed  $T_z^k$  for reproducing the experimental data qualitatively.

Figure 4(a) shows the calculated  $H$ - $T$  phase diagram for  $\mathbf{H}||[100]$ . The calculated transition temperature increases as the field increases even when we take into account only the spin and quadrupole exchange interactions (black dashed curve). It increases up to 20 T (maximum at 16.5 K), decreases above 20 T, and disappears around 75 T. It is noteworthy that the calculated transition temperature emerges again above 80 T and reaches 8 K in our calculations. This reentrant behavior qualitatively explains the phase diagram obtained experimentally [Fig. 1(d)].

This reentrant behavior can be understood by the field dependences of the CEF energies, which are calculated by using the CEF model:  $H_{\text{CEF}} + H_{\text{Zeeman}}$  in the nonordered state [Fig. 4(b)]. The energy splitting of the ground-state doublet by the Zeeman energy is very small for  $\mathbf{H}||[100]$ . The two states of the ground-state doublet gradually separate up to 70 T; however, these states approach again above 70 T and then exhibit a field induced level crossing around 110 T.

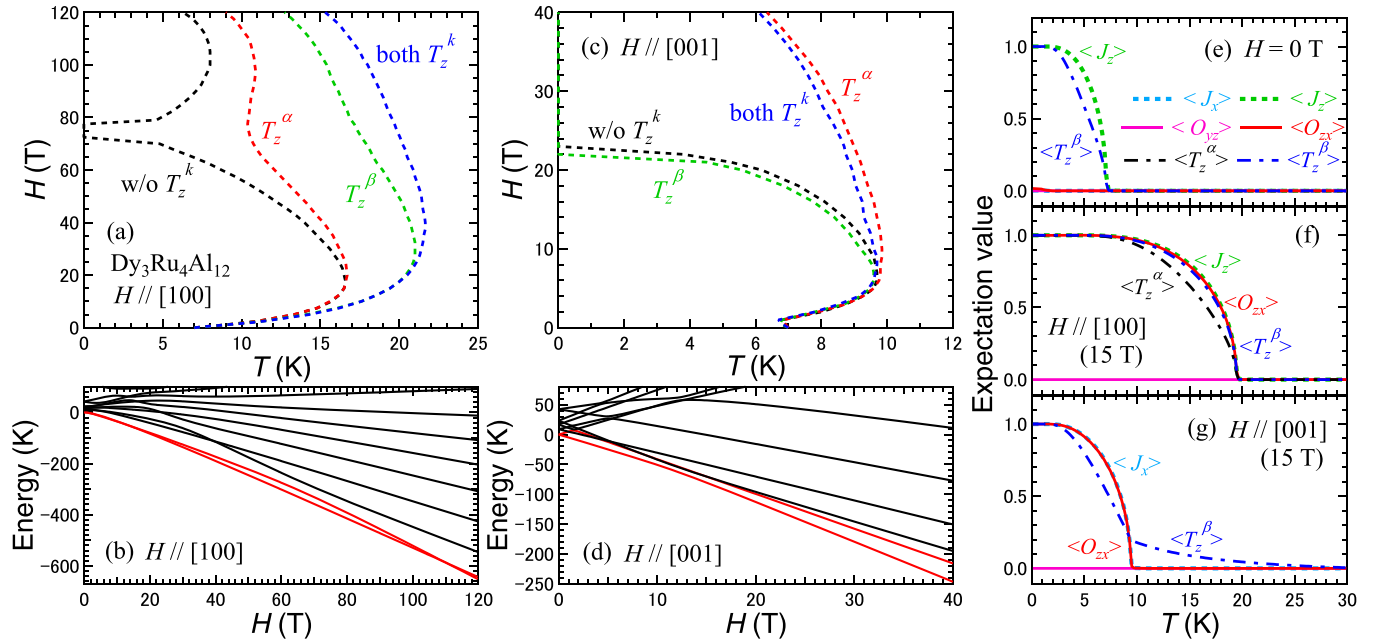


FIG. 4. (a) and (c) The calculated  $H$ - $T$  phase diagram for  $\mathbf{H}||[100]$  (a) and  $\mathbf{H}||[001]$  (c). The phase-transition temperature was evaluated using the spin and quadrupole exchange interactions with or without octupole-mediated interactions in the mean-field approximation, and it corresponds to the emergence of a spontaneous expectation value of  $O_{zx}$ ,  $\langle O_{zx} \rangle$ , in magnetic fields. Here, w/o  $T_z^k$ , without  $T_z^k$ . (b) and (d) The magnetic field dependences of the calculated CEF energies for  $\mathbf{H}||[100]$  (b) and  $\mathbf{H}||[001]$  (d) in the nonordered state. The two states of the ground-state doublet at zero field are depicted by the red solid curves. (e)–(g) Temperature dependences of the expectation values of  $J_x$ ,  $J_z$ ,  $O_{yz}$ ,  $O_{zx}$ ,  $T_z^\alpha$ , and  $T_z^\beta$  at zero magnetic field (e) and a selected field of 15 T applied along [100] (f) and [001] (g). The spontaneous expectation values were normalized at 0.1 K.

Multipole-mediated interactions exist among them by mixing the wave functions of the  $4f$  electronic state by the Zeeman energy. These interactions are enhanced toward the magnetic field of the level crossing, causing the reentrant behavior.

By adding the octupole exchange interactions of  $T_z^k$ , the calculated transition temperature is further enhanced (red, green, and blue dashed curves), suggesting that the octupole-mediated interactions are required to reach the phase-transition temperature of up to 20 K and 40 T [Figs. 1(d) and 4(a)]. Here, the calculated transition temperature depends on the magnitude of  $t_{\text{ex}k}^{AB}$  not experimentally determined, and the reentrant behavior becomes continuous if  $t_{\text{ex}k}^{AB}$  increases. On the other hand, there is a difference between the experimental data and calculations; namely, the magnetic field of the calculated reentrant behavior is larger than the data. This CEF analysis was performed by using a simple mean-field model to avoid failure of convergence due to too many parameters. To clarify the origin of the difference, further theoretical studies including effects of the kagome lattice and anisotropy of the exchange interactions are needed.

For  $\mathbf{H}||[001]$ , the calculated transition temperature decreases up to 1 T and increases above 1 T by applying magnetic fields [Fig. 4(c)]. It rapidly decreases above 10 T and becomes zero above 22 T, when neither  $T_z^k$  is adopted or when  $T_z^\beta$  is adopted (black and green dashed curves). By contrast, the calculated transition temperature survives way beyond 40 T if  $T_z^\alpha$  is induced or if both  $T_z^k$  are induced by applying fields (red and blue dashed curves). Here, the enhancement of  $T_Q$  at low fields in both field directions can be explained by the CEF model with multipole-mediated interactions; that is, the spin (magnetic dipole) interactions alone do not produce this behavior. In this field direction, the ground-state doublet is split by the Zeeman energy, and the excited states approach the ground state up to 12 T [Fig. 4(d)]. The calculated transition temperature displays a maximum around 10 T, because multipole-mediated interactions exist between the ground state and the excited states, which are enhanced as the field increases. Above 12 T, these interactions become weak as reflected in the increment of the energy splitting. Therefore the calculated transition temperature decreases.

Let us try to identify the order parameter for each FIP in terms of spontaneous expectation values of multipole operators. Figures 4(e)–4(g) show the temperature dependences of spontaneous expectation values of  $J_x$ ,  $J_z$ ,  $O_{yz}$ ,  $O_{zx}$ ,  $T_z^\alpha$ , and  $T_z^\beta$  at zero magnetic field and at a field of 15 T in both field directions by assuming nonzero  $T_z^k$ . Here, the expectation value of  $J_y$ ,  $\langle J_y \rangle$ , is always zero, and the uniform components of  $\langle J_x \rangle$  and  $\langle J_z \rangle$  modified by the Zeeman energy are not shown. On cooling in zero field,  $\langle J_z \rangle$  becomes nonzero at  $T_N$  [Fig. 4(e)]. This is consistent with the magnetically ordered structure reported, because the magnetic moments mainly align along [001] [16].  $\langle T_z^\beta \rangle$  appears simultaneously within our calculations.

For  $\mathbf{H}||[100]$ ,  $\langle J_z \rangle$ ,  $\langle O_{zx} \rangle$ ,  $\langle T_z^\alpha \rangle$ , and  $\langle T_z^\beta \rangle$  emerge simultaneously at the calculated transition temperature even at very low fields, and these remain as the field increases [Fig. 4(f)]. The emergence of  $\langle O_{zx} \rangle$  in this field direction is consistent with our previous suggestion that the order parameter is the electric quadrupole  $O_{zx}$  [18]. Because the magnitude of these

values except for  $\langle J_z \rangle$  increases as the field increases (not shown), implying the enhancement of the multipole-mediated interactions, the calculated transition temperature increases at low fields. As described above, the reentrant behavior can be qualitatively explained by the calculation using only the spin and quadrupole exchange interactions. These results suggest that the order parameter of the field induced phase transitions for  $\mathbf{H}||[100]$  is  $O_{zx}$ . The interactions of  $T_z^k$  depending on  $t_{\text{ex}k}^{AB}$  are required to increase the phase-transition temperature reaching up to 20 K and 40 T. Here, the magnetization at 2 K shows no obvious anomaly above 1 T [Fig. 3(d)]. For these reasons, we propose that a plausible order parameter of both FIP-I and FIP-II is  $O_{zx}$  facilitated by the interactions of  $T_z^k$  [Figs. 1(d) and 4(a)].

For  $\mathbf{H}||[001]$ ,  $\langle J_x \rangle$ ,  $\langle O_{yz} \rangle$ ,  $\langle O_{zx} \rangle$ , and  $\langle T_z^\beta \rangle$  emerge at the calculated transition temperature above 1 T. The magnitude of  $\langle O_{yz} \rangle$  decreases as the field increases and becomes zero at 15 T. By contrast,  $\langle J_x \rangle$ ,  $\langle O_{zx} \rangle$ , and  $\langle T_z^\beta \rangle$  continue to be nonzero even above 15 T [Fig. 4(g)]. Here, uniform components by the Zeeman energy are included for  $\langle T_z^\beta \rangle$  and  $\langle T_z^\alpha \rangle$  (not shown) in this field direction. Concerning our previous suggestion that the order parameter of FIP-III is  $O_{yz}$  or  $O_{zx}$ , both quadrupoles may be the order parameter at low fields. However, the magnitude of  $\langle O_{zx} \rangle$  is larger than that of  $\langle O_{yz} \rangle$ , and  $\langle O_{zx} \rangle$  becomes dominant at higher fields.  $C_{44}$ , sensitive to  $O_{zx}$ , shows a large softening toward  $T_Q$  with a more than 6% reduction in the stiffness up to 17 T [Fig. 2(a)]. To produce the magnetic field dependence of  $T_Q(H)$  qualitatively, interactions of  $T_z^k$ , especially  $T_z^\alpha$ , are needed [red and blue dashed curves in Fig. 4(c)]. Here, the magnetization at 2 K is almost saturated at low fields in this field direction [Fig. 3(d)]. From these results, we propose that the order parameter of FIP-III is  $O_{zx}$  facilitated by the interactions of  $T_z^k$  [Figs. 2(b) and 4(c)].

As a result, these experimental data and calculations reveal a magnetic field induced multipolar ordering at very high fields applied along [100] in  $\text{Dy}_3\text{Ru}_4\text{Al}_{12}$ . A plausible order parameter of each FIP is  $O_{zx}$  facilitated by the octupole-mediated interactions of  $T_z^k$ . It is noteworthy that the transition temperature of FIP-II reaches up to 20 K and 40 T. The multipolar ordering in this material at such high temperatures and high magnetic fields is highly interesting.

For  $\mathbf{H}||[001]$ , the calculated transition temperature (red and blue dashed curves) is higher than the experimental data of  $T_Q$ , although  $T_N$  at zero field is reproduced [Figs. 2(b) and 4(c)]. We consider the reason for this discrepancy to be as follows. We previously suggested a geometrically frustrated state of electric quadrupoles due to the kagome lattice, because  $g'_i$  is negative within our CEF analysis [18]. In the present CEF analysis, the data are well explained by negative values of  $g_{\text{ex}i}^{AB} = g'_i$  and  $t_{\text{ex}k}^{AB}$ . If geometrical frustration has an effect on the multipolar system, the phase-transition temperature corresponding to  $T_Q$  should be suppressed. Here, our calculations adopted the orthorhombic CEF model, and geometrical frustration was not considered. For  $\mathbf{H}||[001]$ , the magnetic field does not break the crystal symmetry of the kagome lattice in the (001) plane, and the effect of geometrical frustration can survive up to very high fields. Therefore  $T_Q$  of FIP-III is expected to be suppressed compared with the calculated value.

The emergence of a multipolar ordered state despite magnetic ordering at zero field is similar to that observed in the

kagome-like lattice compounds DyNiAl and ErNiAl [38,39]. The complex magnetic structure below  $T_N$  at zero field in Dy<sub>3</sub>Ru<sub>4</sub>Al<sub>12</sub> [16,21] may be mediated by the multipoles, such as in DyNiAl and ErNiAl [Fig. 4(e)]. In future works, further experiments, such as resonant x-ray scattering, are required to further investigate the ordered state at zero field.

#### IV. CONCLUSION

We conducted ultrasonic and magnetocaloric-effect measurements up to 55.2 T on the distorted kagome-lattice antiferromagnet Dy<sub>3</sub>Ru<sub>4</sub>Al<sub>12</sub>. An obvious softening of  $C_{44}$  was detected above 30 T for  $\mathbf{H}||[100]$ , whereas  $C_{44}$  displays no clear anomaly at very high fields for  $\mathbf{H}||[001]$ . Magnetocaloric-effect measurements indicate the temperature changes during the ultrasonic measurement in pulsed fields. We determined the  $H$ - $T$  phase diagrams for both field directions by using both sets of data in pulsed fields. An exceptional field induced phase transition was found for  $\mathbf{H}||[100]$ . By optimizing the CEF using quadrupole and octupole exchange interactions in the mean-field approximation, the enhancement of  $T_Q$  can be explained, implying that these

multipole-mediated interactions play a crucial role for the magnetic field induced phase transitions. A plausible scenario is that the magnetic field induced phase transitions of FIP-I, FIP-II, and FIP-III are driven by the electric quadrupole  $O_{zx}$  facilitated by the interactions of  $T_z^k$  within our calculations. The effect of geometrical frustration due to the kagome lattice would lower the phase-transition temperature of FIP-III.

#### ACKNOWLEDGMENTS

This work was supported by JSPS KAKENHI Grants No. 18KK0078, No. 18K03507, No. 19K03719, and No. 22K03485. The work was supported by Project No. 21-09766S of the Czech Science Foundation and by MGML [49] within the Program of Czech Research Infrastructures (Project No. LM2018096). We acknowledge the support of the High Magnetic Field Laboratory (HLD) at Helmholtz-Zentrum Dresden-Rossendorf (HZDR), a member of the European Magnetic Field Laboratory (EMFL), the Deutsche Forschungsgemeinschaft (DFG) through SFB 1143, and the Würzburg-Dresden Cluster of Excellence on Complexity and Topology in Quantum Matter ct.qmat (EXC 2147, Project No. 390858490).

- 
- [1] A. P. Ramirez, Strongly geometrically frustrated magnets, *Annu. Rev. Mater. Sci.* **24**, 453 (1994).
- [2] L. Balents, Spin liquids in frustrated magnets, *Nature (London)* **464**, 199 (2010).
- [3] H. Sato, H. Sugawara, Y. Aoki, and H. Harima, Magnetic properties of filled skutterudites, in *Handbook of Magnetic Materials*, edited by K. H. J. Buschow (North-Holland, Amsterdam, 2009), Vol. 18, Chap. 1, pp. 1–110.
- [4] Y. Kuramoto, H. Kusunose, and A. Kiss, Multipole orders and fluctuations in strongly correlated electron systems, *J. Phys. Soc. Jpn.* **78**, 072001 (2009).
- [5] T. Onimaru and H. Kusunose, Exotic quadrupolar phenomena in non-Kramers doublet systems — The cases of PrT<sub>2</sub>Zn<sub>20</sub> ( $T = \text{Ir, Rh}$ ) and PrT<sub>2</sub>Al<sub>20</sub> ( $T = \text{V, Ti}$ )–, *J. Phys. Soc. Jpn.* **85**, 082002 (2016).
- [6] J. Niermann and W. Jeitschko, Ternary rare earth ( $R$ ) transition metal aluminides  $R_3T_4Al_{12}$  ( $T = \text{Ru and Os}$ ) with Gd<sub>3</sub>Ru<sub>4</sub>Al<sub>12</sub> type structure, *Z. Anorg. Allg. Chem.* **628**, 2549 (2002).
- [7] W. Ge, H. Ohta, C. Michioka, and K. Yoshimura, Magnetic properties of the novel layered compounds  $RE_3Ru_4Al_{12}$  ( $RE = \text{La-Nd}$ ), *J. Phys.: Conf. Ser.* **344**, 012023 (2012).
- [8] S. Nakamura, N. Kabeya, M. Kobayashi, K. Araki, K. Katoh, and A. Ochiai, Spin trimer formation in the metallic compound Gd<sub>3</sub>Ru<sub>4</sub>Al<sub>12</sub> with a distorted kagome lattice structure, *Phys. Rev. B* **98**, 054410 (2018).
- [9] T. Matsumura, Y. Ozono, S. Nakamura, N. Kabeya, and A. Ochiai, Helical ordering of spin trimers in a distorted kagome lattice of Gd<sub>3</sub>Ru<sub>4</sub>Al<sub>12</sub> studied by resonant x-ray diffraction, *J. Phys. Soc. Jpn.* **88**, 023704 (2019).
- [10] M. S. Henriques, D. I. Gorbunov, A. V. Andreev, X. Fabrèges, A. Gukasov, M. Uhlarz, V. Petříček, B. Ouladdiaf, and J. Wosnitza, Complex magnetic order in the kagome ferromagnet Pr<sub>3</sub>Ru<sub>4</sub>Al<sub>12</sub>, *Phys. Rev. B* **97**, 014431 (2018).
- [11] D. I. Gorbunov, M. S. Henriques, A. V. Andreev, V. Eigner, A. Gukasov, X. Fabrèges, Y. Skourski, V. Petříček, and J. Wosnitza, Magnetic anisotropy and reduced neodymium magnetic moments in Nd<sub>3</sub>Ru<sub>4</sub>Al<sub>12</sub>, *Phys. Rev. B* **93**, 024407 (2016).
- [12] T. Suzuki, T. Mizuno, K. Takezawa, S. Kamikawa, A. V. Andreev, D. I. Gorbunov, M. S. Henriques, and I. Ishii, Elastic moduli of the distorted kagome-lattice ferromagnet Nd<sub>3</sub>Ru<sub>4</sub>Al<sub>12</sub>, *Phys. B (Amsterdam)* **536**, 18 (2018).
- [13] I. Ishii, T. Mizuno, S. Kumano, T. Umeno, D. Suzuki, A. V. Andreev, D. I. Gorbunov, M. S. Henriques, and T. Suzuki, The crystal electric field effect in the distorted kagome lattice ferromagnet Nd<sub>3</sub>Ru<sub>4</sub>Al<sub>12</sub>, *JPS Conf. Proc.* **30**, 011161 (2020).
- [14] D. I. Gorbunov, M. S. Henriques, A. V. Andreev, Y. Skourski, and M. Dušek, Magnetic, thermal and transport properties of Tb<sub>3</sub>Ru<sub>4</sub>Al<sub>12</sub> with a distorted kagome lattice, *J. Alloys Compd.* **634**, 115 (2015).
- [15] I. Ishii, T. Mizuno, S. Kumano, T. Umeno, D. Suzuki, Y. Kurata, T. Suzuki, D. I. Gorbunov, M. S. Henriques, and A. V. Andreev, Magnetic transition due to the inter-singlet spin-exchange interaction and elastic softening by the interplay of electric quadrupoles in the distorted kagome lattice antiferromagnet Tb<sub>3</sub>Ru<sub>4</sub>Al<sub>12</sub>, *Phys. Rev. B* **101**, 165116 (2020).
- [16] D. I. Gorbunov, M. S. Henriques, A. V. Andreev, A. Gukasov, V. Petříček, N. V. Baranov, Y. Skourski, V. Eigner, M. Paukov, J. Prokleška, and A. P. Gonçalves, Electronic properties of a distorted kagome lattice antiferromagnet Dy<sub>3</sub>Ru<sub>4</sub>Al<sub>12</sub>, *Phys. Rev. B* **90**, 094405 (2014).
- [17] M. S. Henriques, D. I. Gorbunov, D. Kriegner, M. Vališka, A. V. Andreev, and Z. Matěj, Magneto-elastic coupling across the first-order transition in the distorted kagome lattice antiferromagnet Dy<sub>3</sub>Ru<sub>4</sub>Al<sub>12</sub>, *J. Magn. Magn. Mater.* **400**, 125 (2016).
- [18] I. Ishii, T. Mizuno, K. Takezawa, S. Kumano, Y. Kawamoto, T. Suzuki, D. I. Gorbunov, M. S. Henriques, and A. V. Andreev, Magnetic-field-induced quadrupolar ordering and the crystal

- electric field effect in the distorted kagome lattice antiferromagnet  $\text{Dy}_3\text{Ru}_4\text{Al}_{12}$ , *Phys. Rev. B* **97**, 235130 (2018).
- [19] D. I. Gorbunov, T. Nomura, I. Ishii, M. S. Henriques, A. V. Andreev, M. Doerr, T. Stöter, T. Suzuki, S. Zherlitsyn, and J. Wosnitza, Crystal-field effects in the kagome antiferromagnet  $\text{Ho}_3\text{Ru}_4\text{Al}_{12}$ , *Phys. Rev. B* **97**, 184412 (2018).
- [20] D. I. Gorbunov, I. Ishii, Y. Kurata, A. V. Andreev, T. Suzuki, S. Zherlitsyn, and J. Wosnitza, Crystal-field effects in  $\text{Er}_3\text{Ru}_4\text{Al}_{12}$  with a distorted kagome lattice, *Phys. Rev. B* **101**, 094415 (2020).
- [21] S. Gao, M. Hirschberger, O. Zaharko, T. Nakajima, T. Kurumaji, A. Kikkawa, J. Shiogai, A. Tsukazaki, S. Kimura, S. Awaji, Y. Taguchi, T. Arima, and Y. Tokura, Ordering phenomena of spin trimers accompanied by a large geometrical Hall effect, *Phys. Rev. B* **100**, 241115(R) (2019).
- [22] T. Suzuki, I. Ishii, N. Okuda, K. Katoh, T. Takabatake, T. Fujita, and A. Tamaki, Quadrupolar ordering of  $5f$  electrons in  $\text{UCu}_2\text{Sn}$ , *Phys. Rev. B* **62**, 49 (2000).
- [23] Y. Nemoto, T. Yamaguchi, T. Horino, M. Akatsu, T. Yanagisawa, T. Goto, O. Suzuki, A. Dönni, and T. Komatsubara, Ferroquadrupole ordering and  $\Gamma_5$  rattling motion in the clathrate compound  $\text{Ce}_3\text{Pd}_{20}\text{Ge}_6$ , *Phys. Rev. B* **68**, 184109 (2003).
- [24] Y. Nakanishi, T. Sakon, M. Motokawa, M. Ozawa, T. Suzuki, and M. Yoshizawa, Elastic properties and phase diagram of the rare-earth monopnictide  $\text{TbSb}$ , *Phys. Rev. B* **68**, 144427 (2003).
- [25] T. Yanagisawa, T. Goto, Y. Nemoto, S. Miyata, R. Watanuki, and K. Suzuki, Ultrasonic investigation of quadrupole ordering in  $\text{HoB}_2\text{C}_2$ , *Phys. Rev. B* **67**, 115129 (2003).
- [26] T. Goto, Y. Nemoto, K. Sakai, T. Yamaguchi, M. Akatsu, T. Yanagisawa, H. Hazama, K. Onuki, H. Sugawara, and H. Sato, Quadrupolar effect and rattling motion in the heavy-fermion superconductor  $\text{PrOs}_4\text{Sb}_{12}$ , *Phys. Rev. B* **69**, 180511(R) (2004).
- [27] M. Akatsu, T. Goto, O. Suzuki, Y. Nemoto, S. Nakamura, S. Kunii, and G. Kido, Magnetic Anisotropy of the Antiferroquadrupole Phase in  $\text{Ce}_{0.50}\text{La}_{0.50}\text{B}_6$ , *Phys. Rev. Lett.* **93**, 156409 (2004).
- [28] I. Ishii, H. Muneshige, Y. Suetomi, T. K. Fujita, T. Onimaru, K. T. Matsumoto, T. Takabatake, K. Araki, M. Akatsu, Y. Nemoto, T. Goto, and T. Suzuki, Antiferro-quadrupolar ordering at the lowest temperature and anisotropic magnetic field-temperature phase diagram in the cage compound  $\text{PrIr}_2\text{Zn}_{20}$ , *J. Phys. Soc. Jpn.* **80**, 093601 (2011).
- [29] I. Ishii, H. Muneshige, S. Kamikawa, T. K. Fujita, T. Onimaru, N. Nagasawa, T. Takabatake, T. Suzuki, G. Ano, M. Akatsu, Y. Nemoto, and T. Goto, Antiferroquadrupolar ordering and magnetic-field-induced phase transition in the cage compound  $\text{PrRh}_2\text{Zn}_{20}$ , *Phys. Rev. B* **87**, 205106 (2013).
- [30] S. Kamikawa, I. Ishii, K. Takezawa, T. Mizuno, T. Sakami, F. Nakagawa, H. Tanida, M. Sera, T. Suzuki, K. Mitsumoto, and X. Xi, Elastic softening due to the quadrupole interaction and anomalous magnetic phase diagram under the magnetic field in  $\text{HoRu}_2\text{Al}_{10}$ , *Phys. Rev. B* **96**, 155131 (2017).
- [31] I. Ishii, K. Takezawa, T. Mizuno, S. Kamikawa, H. Ninomiya, Y. Matsumoto, S. Ohara, K. Mitsumoto, and T. Suzuki, Ferroquadrupolar ordering due to the quasi-degenerate quartet in the trigonal chiral structure of  $\text{DyNi}_3\text{Ga}_9$ , *J. Phys. Soc. Jpn.* **87**, 013602 (2018).
- [32] I. Ishii, K. Takezawa, T. Mizuno, S. Kumano, T. Suzuki, H. Ninomiya, K. Mitsumoto, K. Umeo, S. Nakamura, and S. Ohara, Anisotropic phase diagram of ferroquadrupolar ordering in the trigonal chiral compound  $\text{DyNi}_3\text{Ga}_9$ , *Phys. Rev. B* **99**, 075156 (2019).
- [33] D. I. Gorbunov, I. Ishii, T. Nomura, M. S. Henriques, A. V. Andreev, M. Uhlarz, T. Suzuki, S. Zherlitsyn, and J. Wosnitza, Magnetic phase diagram and crystal-field effects in the kagome-lattice antiferromagnet  $\text{U}_3\text{Ru}_4\text{Al}_{12}$ , *Phys. Rev. B* **99**, 054413 (2019).
- [34] B. Wolf, B. Lüthi, S. Schmidt, H. Schwenk, M. Sieling, S. Zherlitsyn, and I. Kouroudis, New experimental techniques for pulsed magnetic fields – ESR and ultrasonics, *Phys. B (Amsterdam)* **294-295**, 612 (2001).
- [35] S. Zherlitsyn, B. Wustmann, T. Herrmannsdörfer, and J. Wosnitza, Magnet-technology development at the Dresden high magnetic field laboratory, *J. Low Temp. Phys.* **170**, 447 (2013).
- [36] Y. Kohama, C. Marcenat, T. Klein, and M. Jaime, AC measurement of heat capacity and magnetocaloric effect for pulsed magnetic fields, *Rev. Sci. Instrum.* **81**, 104902 (2010).
- [37] T. Kihara, Y. Kohama, Y. Hashimoto, S. Katsumoto, and M. Tokunaga, Adiabatic measurements of magneto-caloric effects in pulsed high magnetic fields up to 55 T, *Rev. Sci. Instrum.* **84**, 074901 (2013).
- [38] I. Ishii, D. Suzuki, T. Umeno, Y. Kurata, Y. Wada, T. Suzuki, A. V. Andreev, D. I. Gorbunov, A. Miyata, S. Zherlitsyn, and J. Wosnitza, Distinct field-induced ferroquadrupolar states for two different magnetic-field directions in  $\text{DyNiAl}$ , *Phys. Rev. B* **103**, 195151 (2021).
- [39] I. Ishii, Y. Kurata, Y. Wada, M. Nohara, T. Suzuki, K. Araki, and A. V. Andreev, Ferroquadrupolar ordering in a magnetically ordered state in  $\text{ErNiAl}$ , *Phys. Rev. B* **105**, 165147 (2022).
- [40] M. T. Hutchings, Point-charge calculations of energy levels of magnetic ions in crystalline electric fields, *Solid State Phys.* **16**, 227 (1964).
- [41] R. Shiina, H. Shiba, and P. Thalmeier, Magnetic-field effects on quadrupolar ordering in a  $\Gamma_8$ -quartet system  $\text{CeB}_6$ , *J. Phys. Soc. Jpn.* **66**, 1741 (1997).
- [42] M. Sera, H. Nohara, M. Nakamura, H. Tanida, T. Nishioka, and M. Matsumura, Unusual temperature-dependent exchange interaction in  $\text{GdFe}_2\text{Al}_{10}$  in comparison with  $\text{GdRu}_2\text{Al}_{10}$ , *Phys. Rev. B* **88**, 100404(R) (2013).
- [43] B. Lüthi, Interaction of magnetic ions with phonons, in *Dynamical Properties of Solids*, edited by G. K. Horton and A. A. Maradudin (North-Holland, Amsterdam, 1980), Vol. 3, Chap. 4, pp. 245–292.
- [44] See Supplemental Material of Ref. [32].
- [45] Y. P. Varshni, Temperature dependence of the elastic constants, *Phys. Rev. B* **2**, 3952 (1970).
- [46] Z. Zhang, V. Keppens, and T. Egami, A simple model to predict the temperature dependence of elastic moduli of bulk metallic glasses, *J. Appl. Phys.* **102**, 123508 (2007).
- [47] N. Van Hieu, T. Takeuchi, H. Shishido, C. Tonohiro, T. Yamada, H. Nakashima, K. Sugiyama, R. Settai, T. D. Matsuda, Y. Haga, M. Hagiwara, K. Kindo, S. Araki, Y. Nozue, and Y. Ōnuki, Magnetic properties and crystalline electric field scheme in  $\text{RRhIn}_5$  (R: Rare Earth), *J. Phys. Soc. Jpn.* **76**, 064702 (2007).
- [48] S. Kamikawa, I. Ishii, Y. Noguchi, H. Goto, T. K. Fujita, F. Nakagawa, H. Tanida, M. Sera, and T. Suzuki, Elastic softening in  $\text{HoFe}_2\text{Al}_{10}$  due to the quadrupole interaction under an orthorhombic crystal electric field, *J. Phys. Soc. Jpn.* **85**, 074604 (2016).
- [49] See <https://mgml.eu>